

**Achieving synergistic improvement in dielectric and energy storage properties at
high-temperature of all-organic copolymers via physical electrostatic effect**

Yanan Shang^{a,b}, Yu Feng^{a,b*}, Zhaotong Meng^{a,b}, Changhai Zhang^{a,b}, Tiandong
Zhang^{a,b}, Qingguo Chi^{a,b*}

^aKey Laboratory of Engineering Dielectrics and Its Application, Ministry of
Education, Harbin University of Science and Technology, Harbin 150080, PR China

^bSchool of Electrical and Electronic Engineering, Harbin University of Science and
Technology, Harbin 150080, PR China

Correspondence

Email: fengyu@hrbust.edu.cn and qgchi@hotmail.com

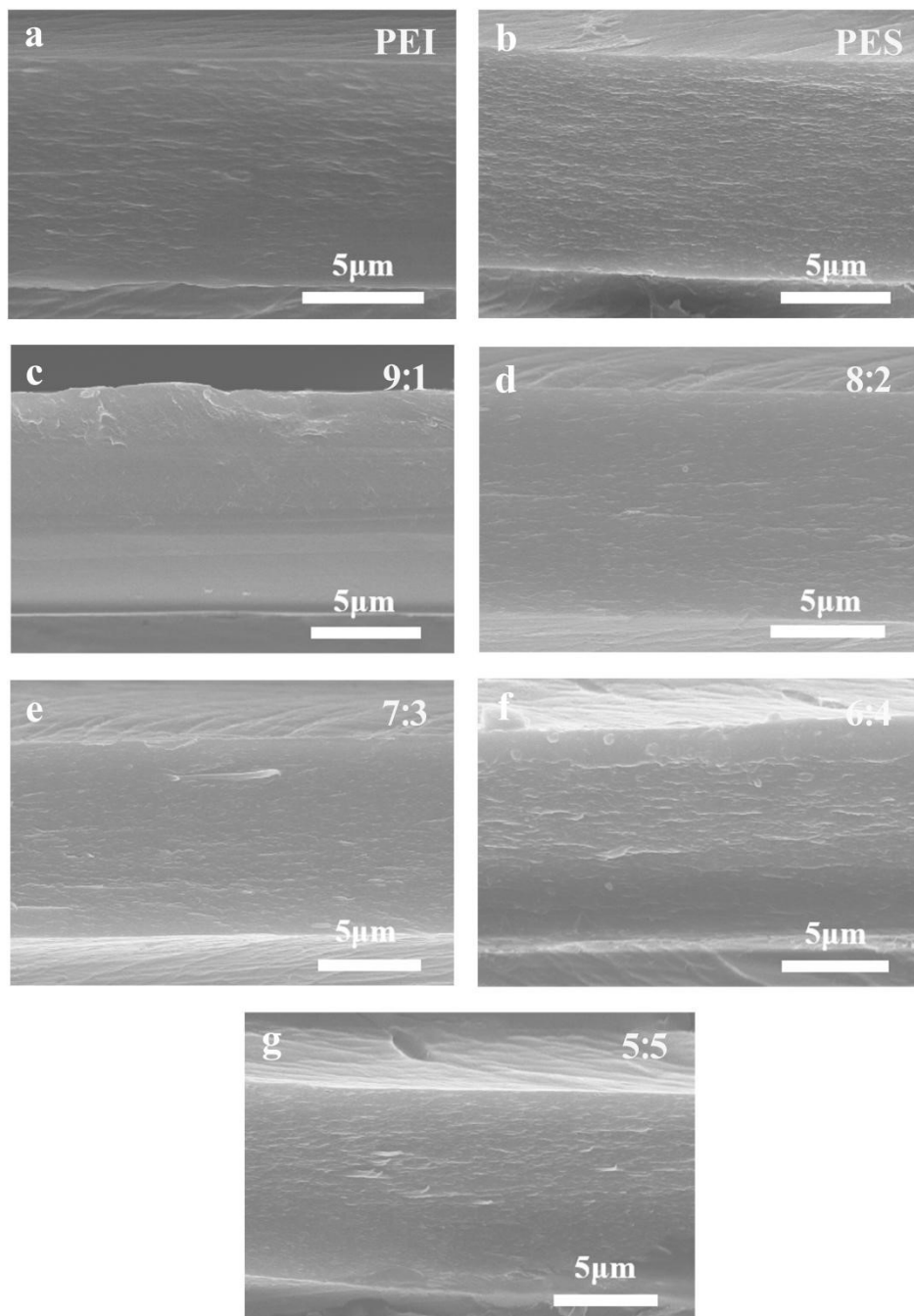


Fig.S1 SEM images of cross-section of the all-organic composite dielectrics.

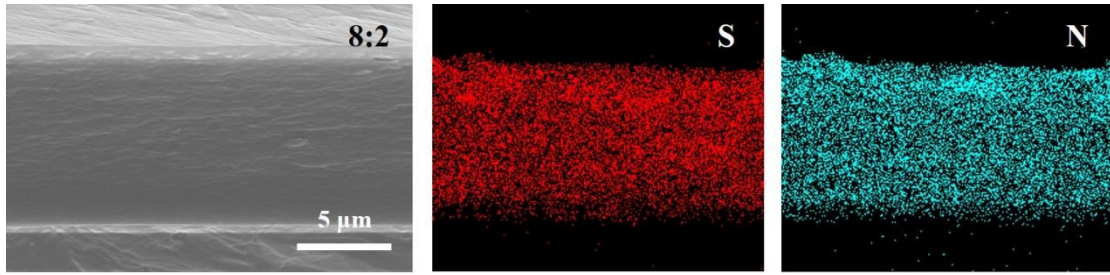


Fig.S2 SEM image and distribution of S and N elements in the cross-section.

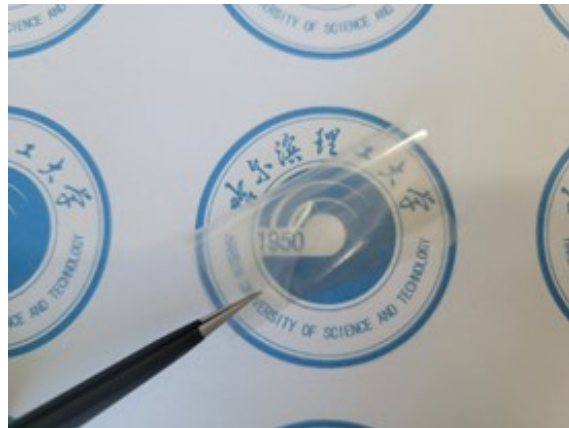


Fig.S3 optical photograph of the composite film.

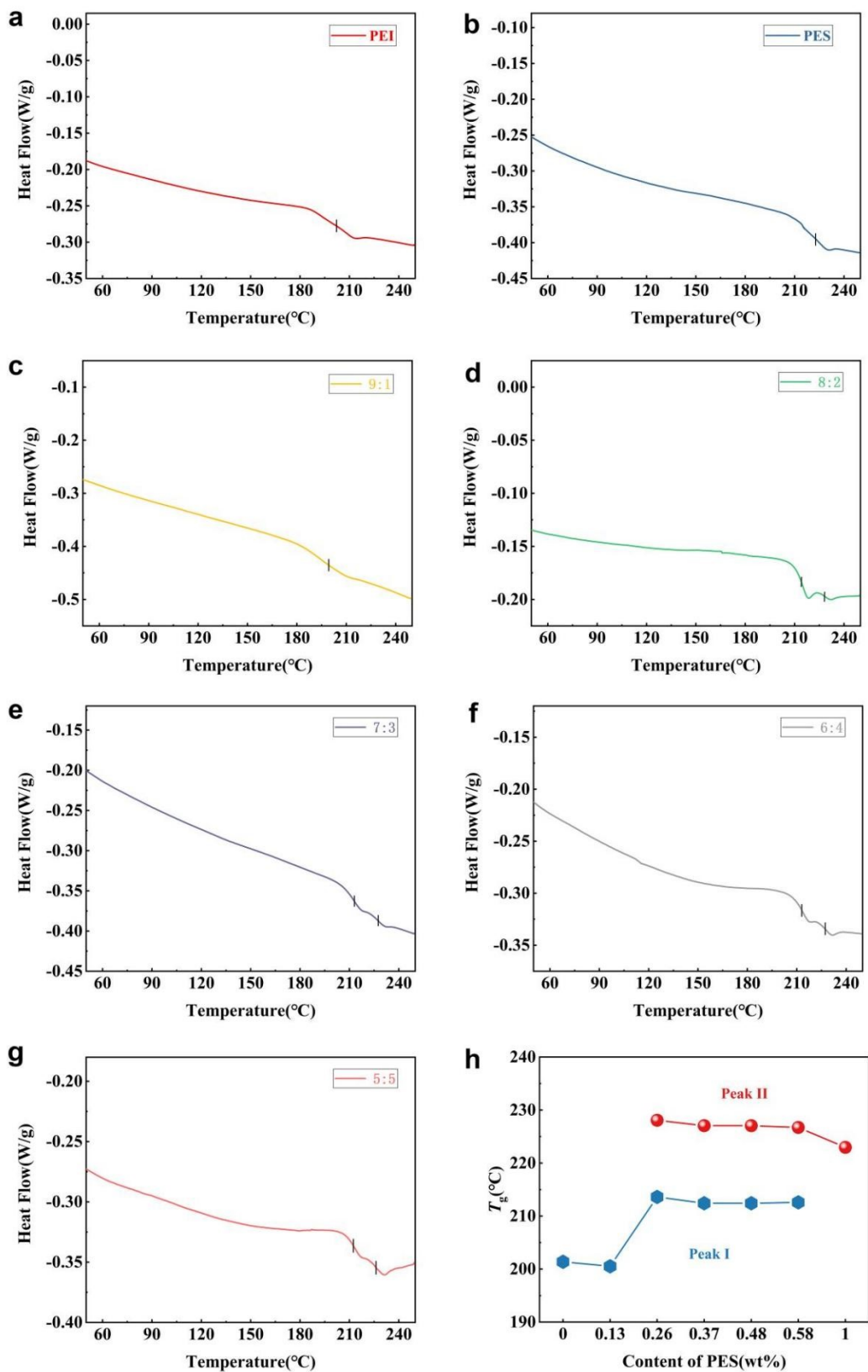


Fig.S4 DSC curves of (a) PEI; (b) PES; (c) 9:1; (d) 8:2; (e) 7:3; (f) 6:4; (g) 5:5; and (h)

T_g of peak I and peak II.

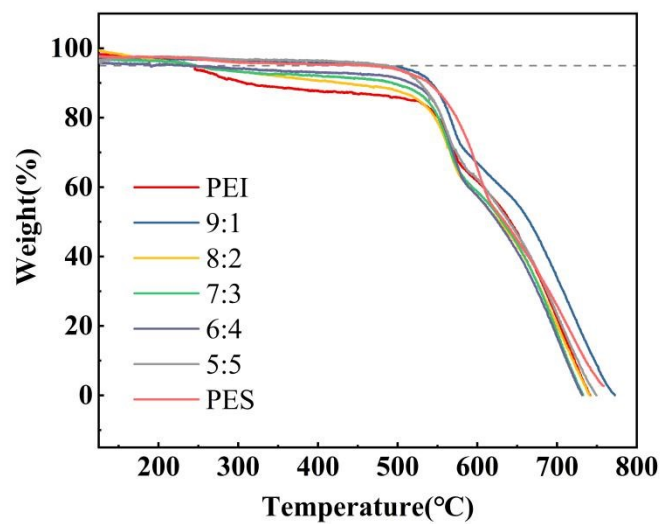


Fig.S5 TGA of the organic-organic composite dielectrics.

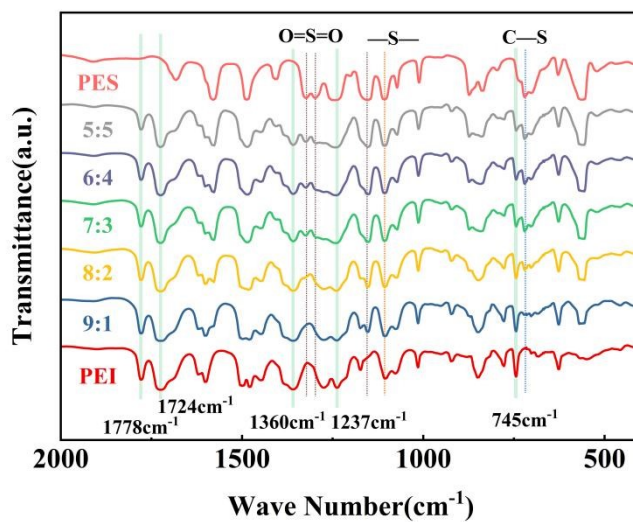


Fig.S6 FTIR spectra of the organic-organic composite dielectrics.

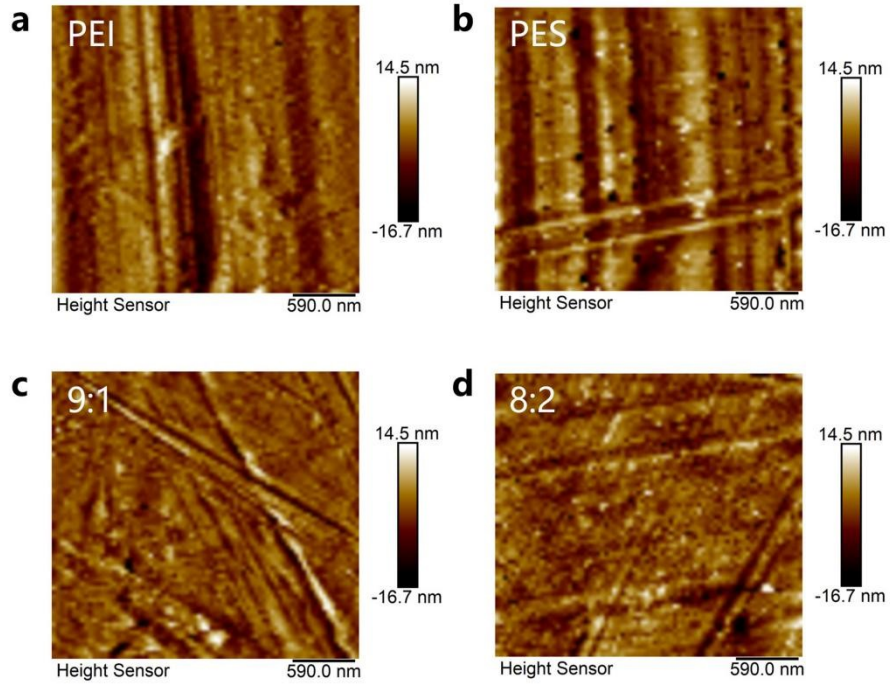


Fig.S7 AFM images of (a) PEI; (b) PES; (c) the 9:1 and (d) the 8:2 composite dielectrics.

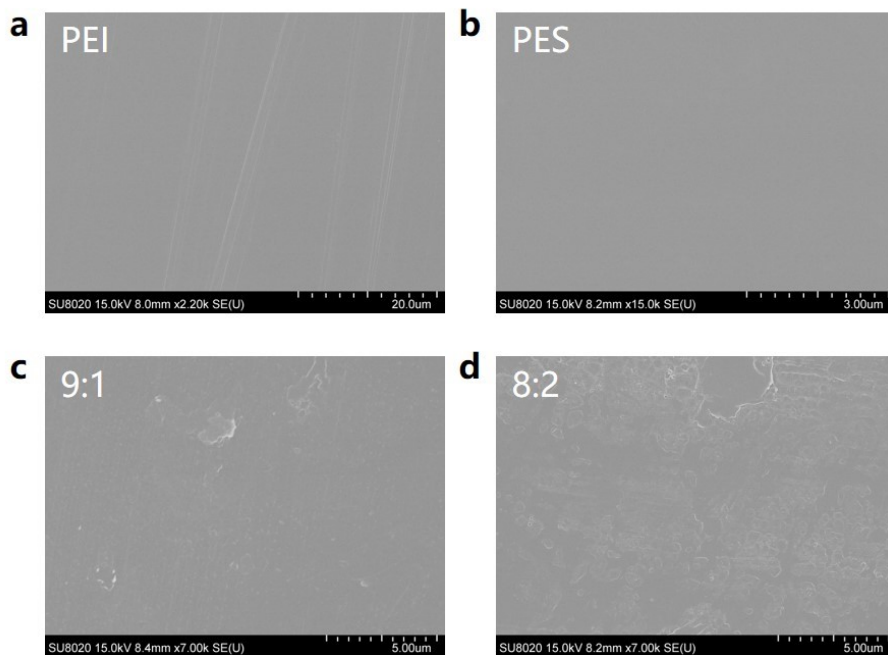


Fig.S8 Surface SEM images of (a) PEI; (b) PES; (c) the 9:1 and (d) the 8:2 composite dielectrics.

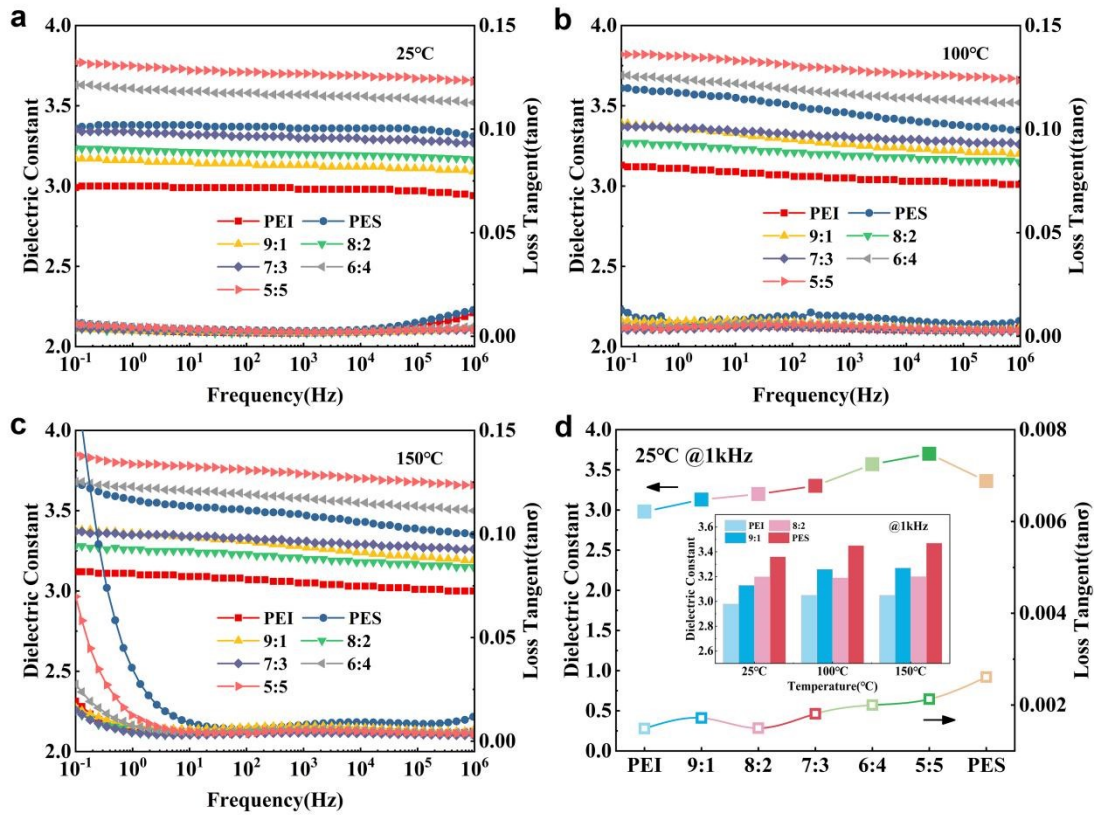


Fig.S9 Frequency dependence of the dielectric constant and loss tangent at (a) 25°C, (b) 100°C, and (c) 150°C; (d) dielectric constant and loss tangent at 1 kHz of the organic-organic composite dielectrics.

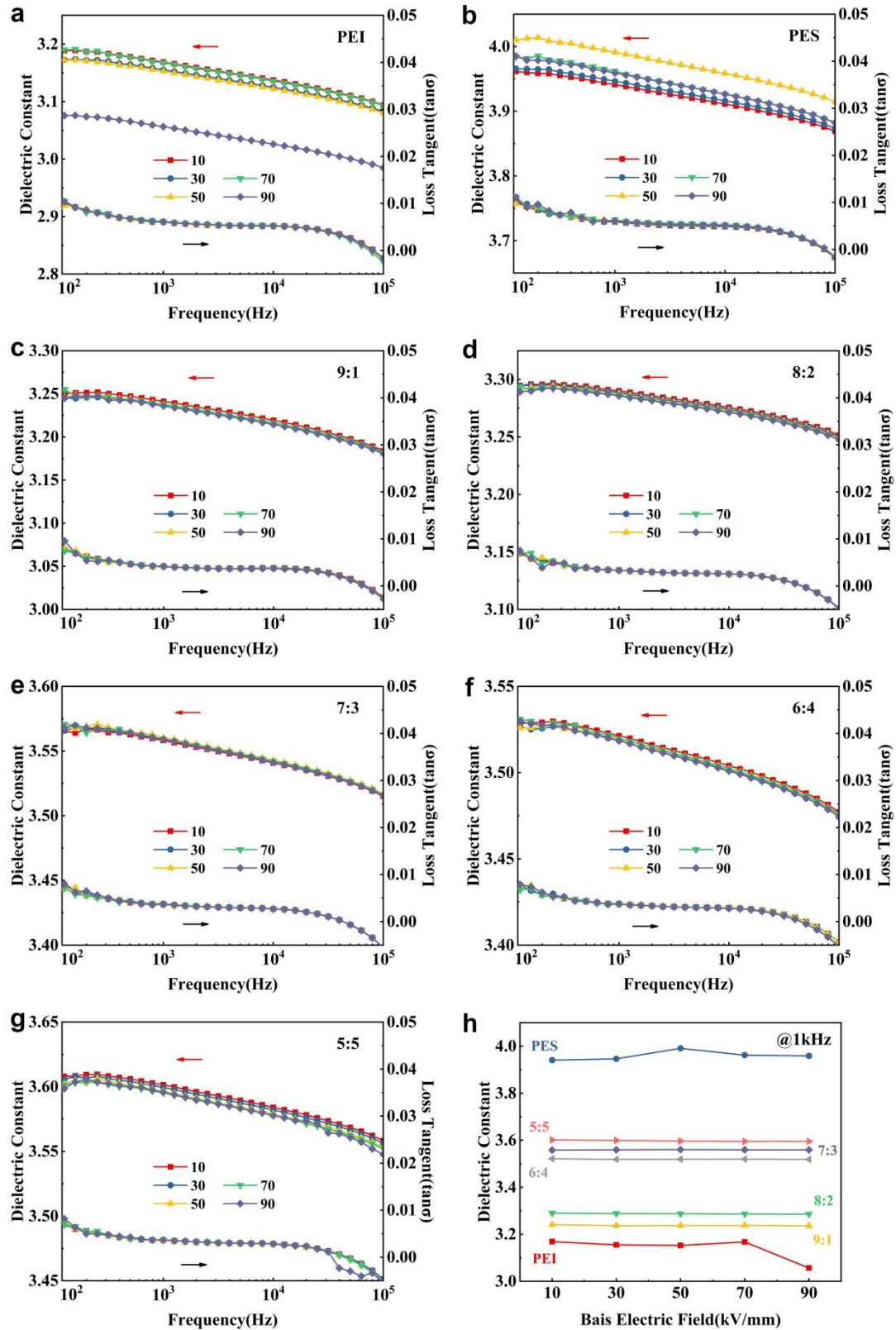


Fig.S10 Frequency dependence of dielectric constant and loss tangent at DC bias of (a) PEI; (b) PES; (c) the 9:1; (d) the 8:2; (e) the 7:3; (f) the 6:4; (g) the 5:5 and (h) variation of dielectric constant with electric field.

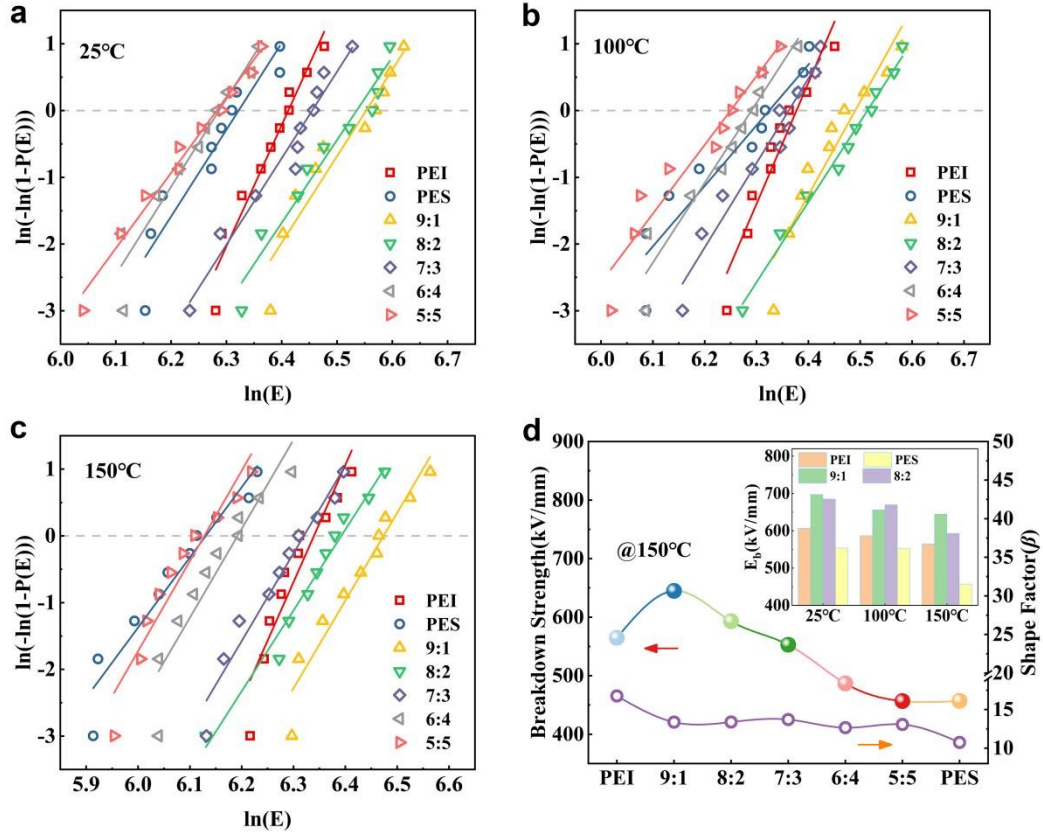


Fig.S11 Weibull breakdown distribution at (a) 25°C, (b) 100°C, and (c) 150°C; (d) breakdown strength and shape factor of the organic-organic composite dielectrics.

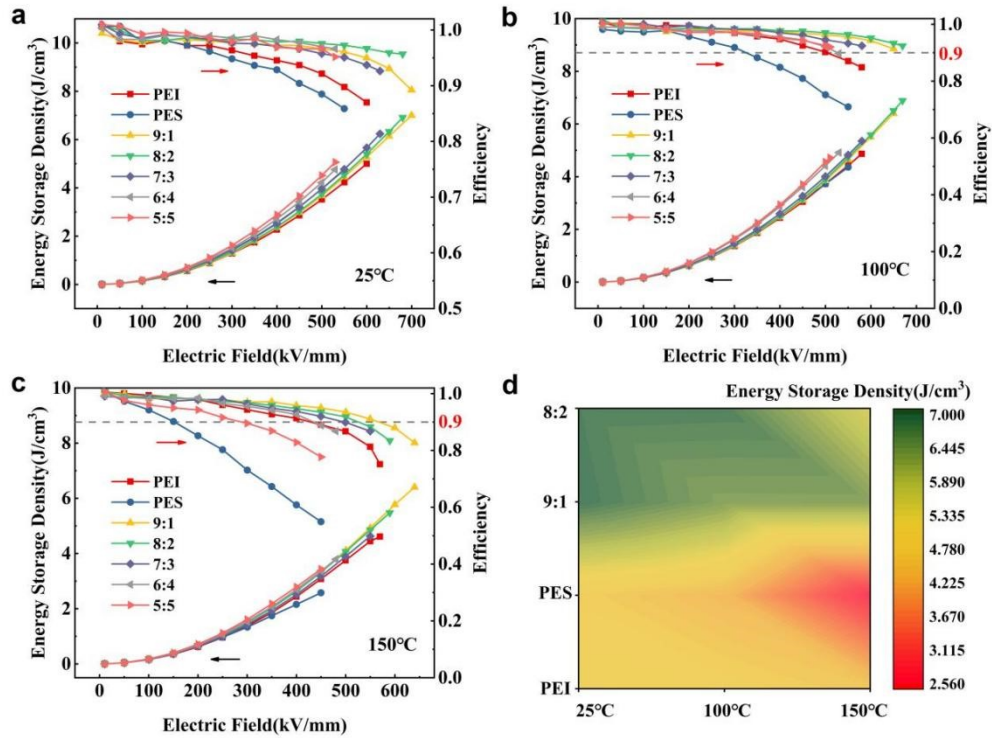


Fig.S12 Energy storage properties at (a) 25°C, (b) 100°C, and (c) 150°C; (d) contour map of energy storage density of the organic-organic composite dielectrics.

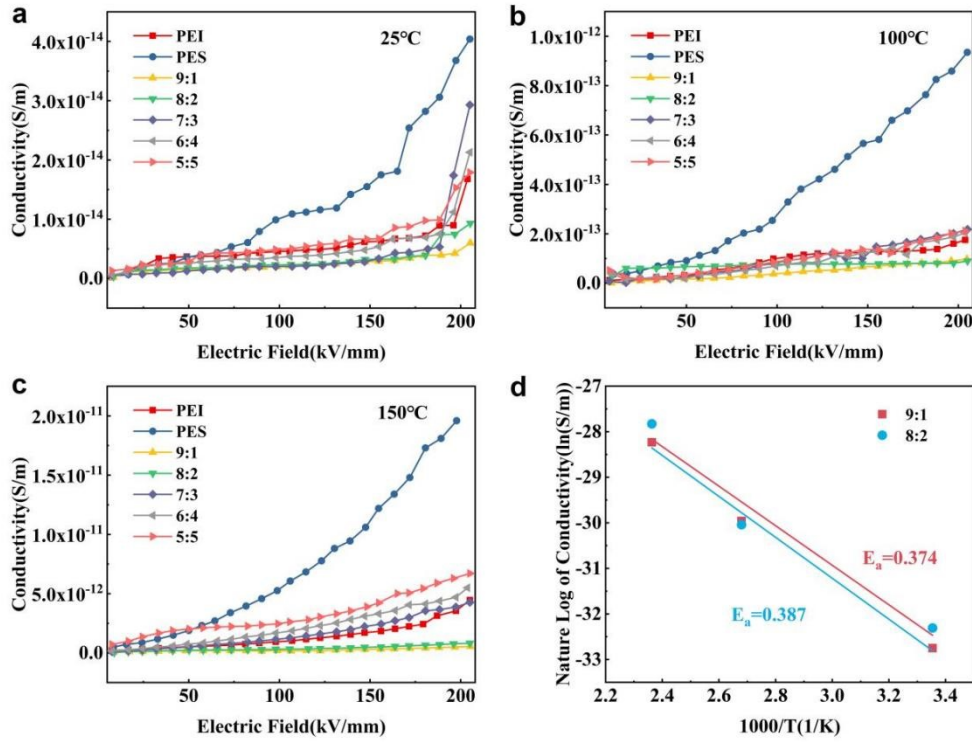


Fig.S13 Conductivity of the organic-organic composite dielectrics at (a) 25°C, (b) 100°C, and (c) 150°C; (d) activation energy of 9:1 and 8:2 composite dielectrics.

Conduction mechanism ^[1-4]

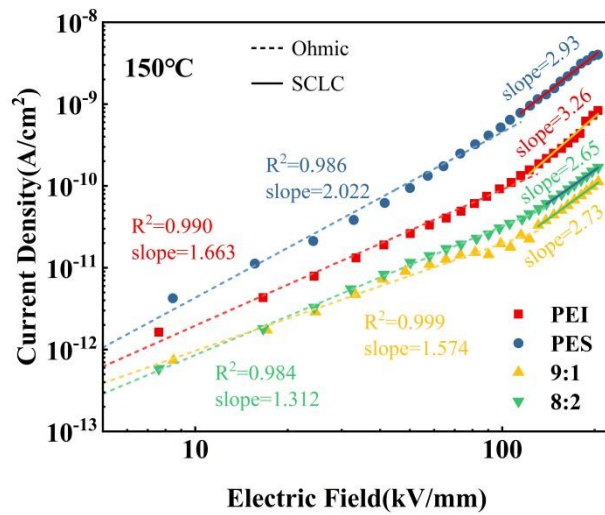


Fig.S14 Ohmic conduction and space charge limited current fitting.

Ohmic conduction

$$J = \sigma E \quad (S1)$$

where σ is the DC conductivity and E is the applied electric field. In the ohmic conduction model, the current density J is proportional to the electric field E . In Fig.S14, from 0 to 100 kV mm⁻¹, the slope of all data fits is greater than 1, so the Ohmic conduction model is not applicable.

Space charge limited current

$$J = \frac{9\mu\epsilon_r\epsilon_0 U^2}{8d^3} \quad (\text{S2})$$

where μ is the carrier mobility, ϵ_r is the dielectric constant, ϵ_0 is the vacuum dielectric constant, U is the applied voltage and d is the thickness of the sample. In Eq. S2, the current density J is positively related to the square of E . In contrast, in Fig.S14, from 100 to 200 kV mm⁻¹, the slopes of the fitted straight lines are all greater than 2. Therefore, the space charge-limited current model is not applicable.

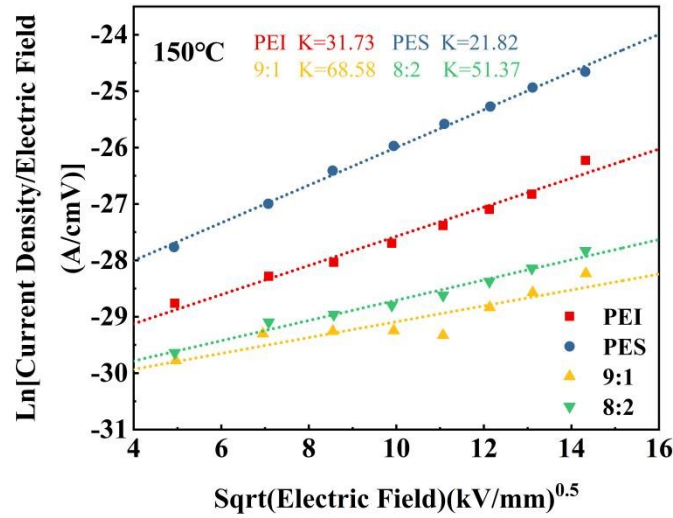


Fig.S15 Poole-Frenke emission fitting.

Poole-Frenke emission

$$J = \sigma_0 E \exp\left(\frac{-\mu_{\text{PF}} + e\sqrt{eE/\pi\epsilon_r\epsilon_0}}{K_B T}\right) \quad (\text{S3})$$

where σ_0 is the conductivity, E is the applied electric field, μ_{PF} is the trap barrier

height, e is the elementary charge, ϵ_r is the dielectric constant, ϵ_0 is the vacuum dielectric constant, K_B is the Boltzmann constant and T is the temperature.

Eq. S3 takes logarithms on both sides and can be deformed as:

$$\ln\left(\frac{J}{E}\right) = \ln(\sigma_0) - \left(\frac{\mu_{PF}}{K_B T}\right) + \left(\frac{e\sqrt{e/\pi\epsilon_r\epsilon_0}}{K_B T}\right)\sqrt{E} \quad (S4)$$

It can be seen that $\ln(J/E)$ is positively related to $E^{0.5}$. The P-F emission fitting results are shown in Fig.S15, and although the data points are well fitted, the value of k calculated from the slopes differs by an order of magnitude from the experimental data, so the P-F emission model is not applicable either.

Schottky emission

$$J = A_R T^2 \exp\left(\frac{-\phi_B + e\sqrt{eE/4\pi\epsilon_r\epsilon_0}}{K_B T}\right) \quad (S5)$$

where A_R is the effective Richardson constant, ϕ_B is the interface energy barrier height, e is the elementary charge, E is the applied electric field, ϵ_r is the dielectric constant, ϵ_0 is the vacuum dielectric constant and K_B is the Boltzmann constant and T is the temperature. Eq. S5 can be deformed as:

$$\ln\left(\frac{J}{T^2}\right) = \ln(A_R) - \left(\frac{\phi_B}{K_B T}\right) + \left(\frac{e\sqrt{e/4\pi\epsilon_r\epsilon_0}}{K_B T}\right)\sqrt{E} \quad (S6)$$

$\ln(J/T^2)$ is positively related to $E^{0.5}$. The results of the Schottky emission fitting are shown in Fig.S16, where the data points are well fitted and the value of ϵ_r calculated from the slope is consistent with the experimental data, thus the low field is consistent with the Schottky emission model.

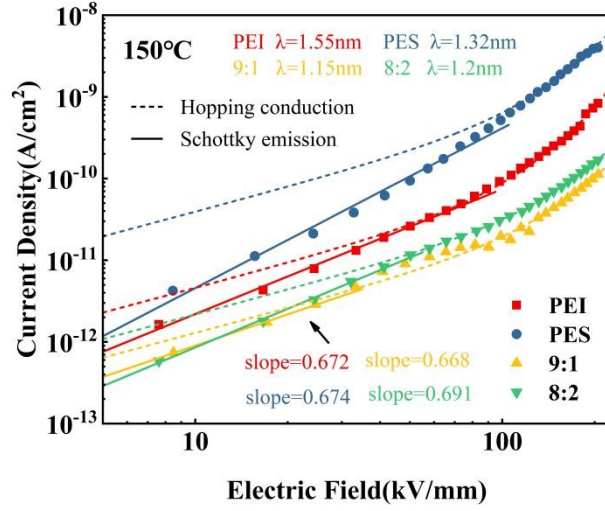


Fig.S16 Schottky emission and hopping conduction fitting.

Hopping conduction model

$$J(E, T) = 2ne\lambda v \cdot \exp\left(-\frac{W_a}{K_B T}\right) \cdot \sinh\left(\frac{\lambda e E}{2K_B T}\right) \quad (S7)$$

where n is the carrier concentration, e is the charge of the carriers, λ is the hopping distance, v is the attempt-to-escape frequency, W_a is the activation energy, and K_B is the Boltzmann constant and T is the temperature. That can be simplified as:

$$J = A * \sinh(B * x) \quad (S8)$$

where A and B are two lumped parameters. The frequency hopping conduction model was well fitted with λ of 1.55nm, 1.32nm, 1.15nm and 1.2nm for PEI, PES, 9:1 and 8:2 composites, respectively.

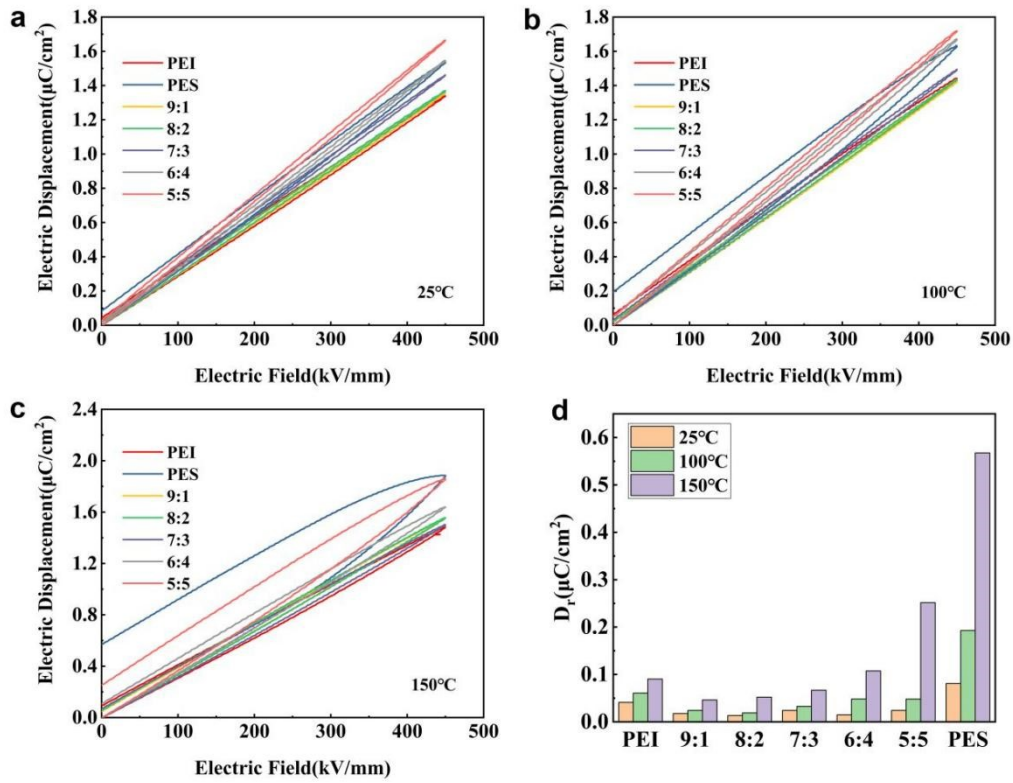


Fig.S17 D - E loops at (a) 25°C, (b) 100°C, and (c) 150°C; (d) D_r of the organic-organic composite dielectrics at 25°C, 100°C and 150 °C.

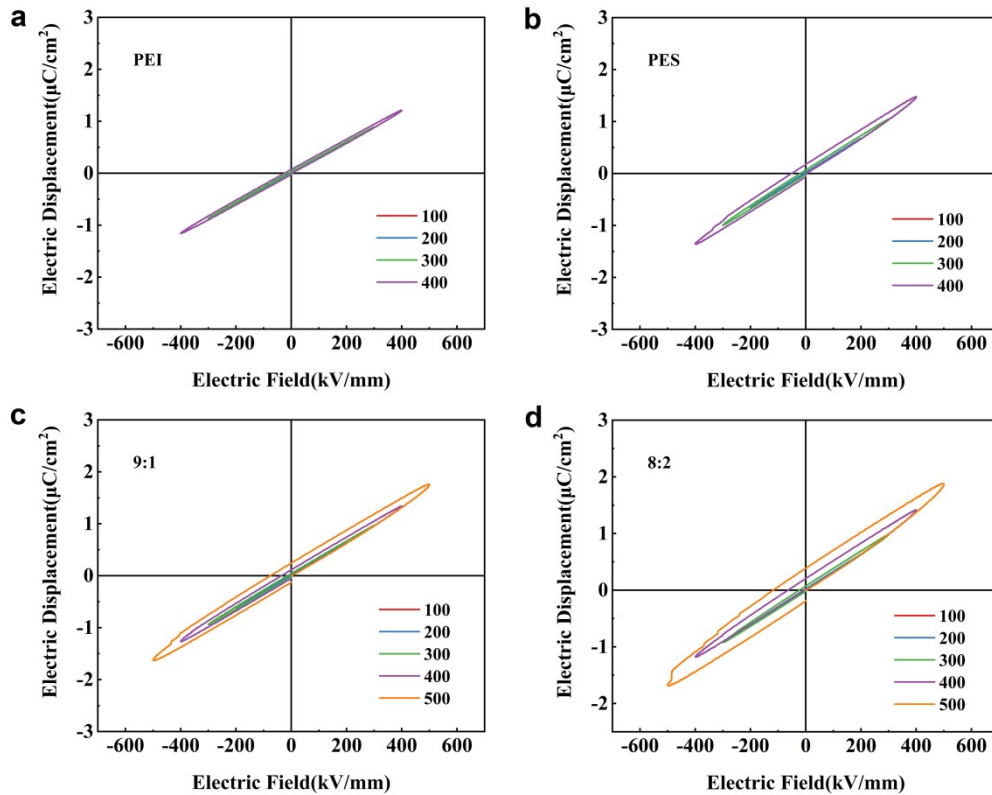


Fig.S18 D - E loops of (a) PEI; (b) PES; (c) the 9:1 and (d) the 8:2 composite dielectrics under sine signal at 25°C.

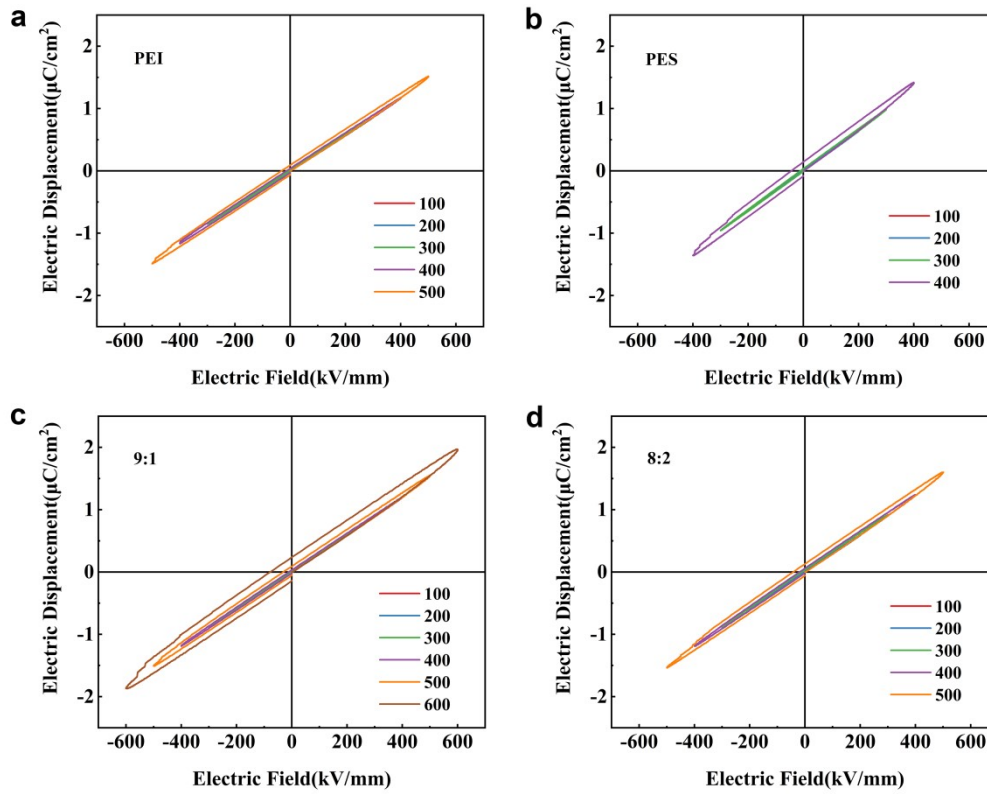


Fig.S19 D - E loops of (a) PEI; (b) PES; (c) the 9:1 and (d) the 8:2 composite dielectrics under sine signal at 100°C.

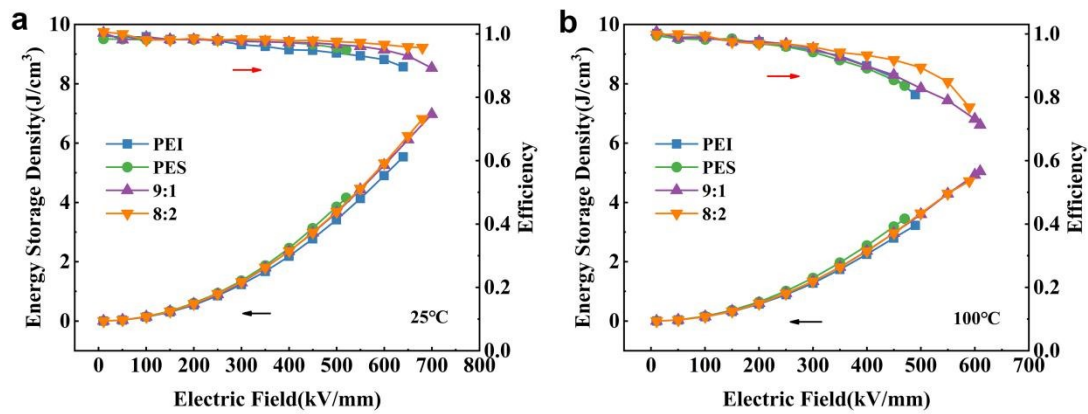


Fig.S20 Energy storage properties under triangle wave at (a) 25°C and (b) 100°C.

References

- [1] H. Li, B. S. Chang, H. Kim, Z. L. Xie, A. Lainé, L. Ma, T. L. Xu, C. Q. Yang, J. Kwon, S. W. Shelton, L. M. Klivansky, V. Altoé, B. Gao, A. M. Schwartzberg, Z. R. Peng, R. O. Ritchie, T. Xu, M. Salmeron, R. Ruiz, K. Barry Sharpless, P. Wu,

- Y. Liu, *Joule*, 2023, **7**(1), 95-111.
- [2] M. C. Yang, S. J. Wang, J. Fu, Y. J. Zhu, J. J. Liang, S. Cheng, S. X. Hu, J. Hu, J. L. He, Q. Li, *Adv. Mater.*, 2301936.
- [3] J. F. Dong, L. Li, P. Q. Qiu, Y. P. Pan, Y. J. Niu, L. Sun, Z. Z. Pan, Y. Q. Liu, L. Tan, X. W. Xu, C. Xu, G. F. Luo, Q. Wang, H. Wang, *Adv. Mater.*, 2023, **35**(20), 2211487.
- [4] J. H. Song, H. M. Qin, S. Y. Qin, M. Liu, S. X. Zhang, J. Y. Chen, Y. Zhang, S. Wang, Q. Li, L. J. Dong, C. X. Xiong, *Mater. Horiz.*, 2023, **10**, 2139-2148.